

# Creating, moving and merging Dirac points with a Fermi gas in a tunable honeycomb lattice

Leticia Tarruell, Daniel Greif, Thomas Uehlinger, Gregor Jotzu and Tilman Esslinger  
*Institute for Quantum Electronics, ETH Zurich, 8093 Zurich, Switzerland*

PACS numbers: 03.75.Ss, 05.30.Fk, 67.85.Lm, 71.10.Fd, 73.22.Pr

Dirac points lie at the heart of many fascinating phenomena in condensed matter physics, from massless electrons in graphene to the emergence of conducting edge states in topological insulators [1, 2]. At a Dirac point, two energy bands intersect linearly and the particles behave as relativistic Dirac fermions. In solids, the rigid structure of the material sets the mass and velocity of the particles, as well as their interactions. A different, highly flexible approach is to create model systems using fermionic atoms trapped in the periodic potential of interfering laser beams, a method which so far has only been applied to explore simple lattice structures [3, 4]. Here we report on the creation of Dirac points with adjustable properties in a tunable honeycomb optical lattice. Using momentum-resolved interband transitions, we observe a minimum band gap inside the Brillouin zone at the position of the Dirac points. We exploit the unique tunability of our lattice potential to adjust the effective mass of the Dirac fermions by breaking inversion symmetry. Moreover, changing the lattice anisotropy allows us to move the position of the Dirac points inside the Brillouin zone. When increasing the anisotropy beyond a critical limit, the two Dirac points merge and annihilate each other – a situation which has recently attracted considerable theoretical interest [5–9], but seems extremely challenging to observe in solids [10]. We map out this topological transition in lattice parameter space and find excellent agreement with *ab initio* calculations. Our results not only pave the way to model materials where the topology of the band structure plays a crucial role, but also provide an avenue to explore many-body phases resulting from the interplay of complex lattice geometries with interactions [11, 12].

Ultracold Fermi gases have emerged as a versatile tool to simulate condensed matter phenomena [3, 4, 13]. For example, the control of interactions in optical lattices has lead to the observation of Mott insulating phases [14, 15], providing new access to the physics of strongly correlated materials. However, the topology of the band structure is equally important for the properties of a solid. A prime example is the honeycomb lattice of graphene, where the presence of topological defects in momentum

space – the Dirac points – leads to extraordinary transport properties, even in the absence of interactions [1]. In

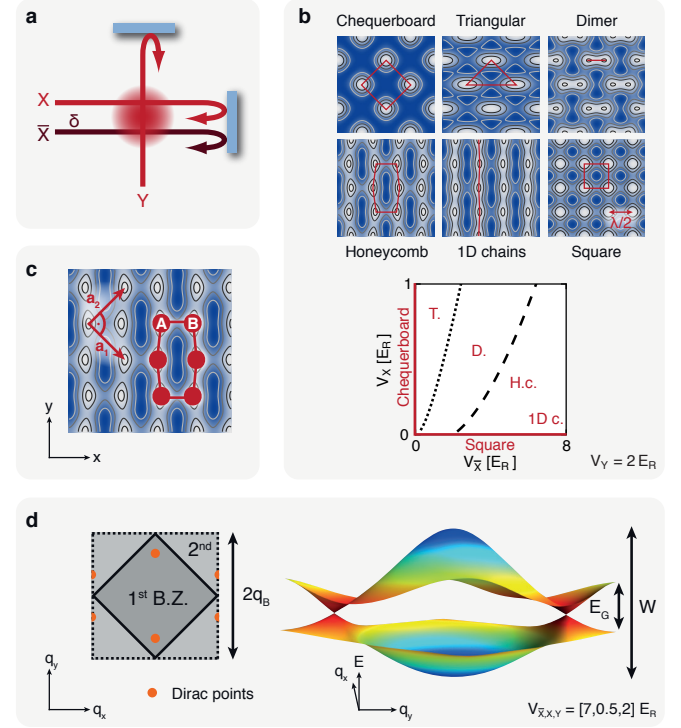


**FIG. 1: Optical lattice with adjustable geometry.** **a**, Three retro-reflected laser beams of wavelength  $\lambda = 1064$  nm create the two-dimensional lattice potential of equation (1).  $X$  and  $Y$  interfere and produce a checkerboard pattern, while  $\bar{X}$  creates an independent standing wave. Their relative position is controlled by the detuning  $\delta$ . **b**, Different lattice potentials can be realised depending on the intensities of the lattice beams, as displayed above. The diagram below shows the accessible lattice geometries as a function of the lattice depths  $V_{\bar{X}}$  and  $V_X$ . The transition between triangular (T.) and dimer (D.) lattices is indicated by a dotted line. When crossing the dashed line into the honeycomb (H.c.) regime, Dirac points appear. The limit  $V_{\bar{X}} \gg V_{X,Y}$  corresponds to weakly coupled one-dimensional chains (1D c.). **c**, The real space potential of the honeycomb lattice has a 2-site unit cell (A,B sites) and the primitive lattice vectors are perpendicular. **d**, Sketch of the first and second Brillouin zones (B.Z.) of the honeycomb lattice, indicating the position of the Dirac points. On the right, a three dimensional view of the energy spectrum shows the linear intersection of the bands at the two Dirac points. We denote the full bandwidth  $W$ , and the minimum energy gap at the edges of the Brillouin zone  $E_G$ .

quantum gases, a honeycomb lattice has recently been realised and investigated with a Bose-Einstein condensate [16, 17], but no signatures of Dirac points were observed. Here we study an ultracold Fermi gas of  $^{40}\text{K}$  atoms in a two-dimensional tunable optical lattice, which can be continuously adjusted to create square, triangular, dimer and honeycomb structures. In the honeycomb lattice, we identify the presence of Dirac points in the band structure by observing a minimum band gap inside the Brillouin zone via interband transitions. Our method is closely related to a technique recently used with bosonic atoms to characterize the linear crossing of two high-energy bands in a one-dimensional bichromatic lattice [18], but provides in addition momentum resolution.

To create and manipulate Dirac points, we have developed a two-dimensional optical lattice of adjustable geometry. It is formed by three retro-reflected laser beams of wavelength  $\lambda = 1064$  nm, arranged as depicted in Fig. 1a. The interference of two perpendicular beams  $X$  and  $Y$  gives rise to a chequerboard lattice of spacing  $\lambda/\sqrt{2}$ . A third beam  $\bar{X}$ , collinear with  $X$  but detuned by a frequency  $\delta$ , creates an additional standing wave of spacing  $\lambda/2$ . This yields a potential of the form

$$V(x, y) = -V_{\bar{X}} \cos^2(kx + \theta/2) - V_X \cos^2(kx) \\ - V_Y \cos^2(ky) - 2\alpha \sqrt{V_X V_Y} \cos(kx) \cos(ky) \cos \varphi(1)$$

where  $V_{\bar{X}}$ ,  $V_X$  and  $V_Y$  denote the single beam lattice depths (proportional to the laser beam intensities),  $\alpha$  is the visibility of the interference pattern and  $k = 2\pi/\lambda$ . We can adjust the two phases continuously, and choose  $\theta = \pi$  and  $\varphi = 0$  (see Methods). Varying the relative intensities of the beams allows us to realise various lattice structures, as displayed in Fig. 1b. In the following we focus on the honeycomb lattice, whose real space potential is shown in Fig. 1c.

The honeycomb lattice consists of two sublattices  $A$  and  $B$ . Therefore, the wavefunctions are two-component spinors. Tunneling between the sublattices leads to the formation of two energy bands, which are well separated from the higher bands and have a conical intersection at two quasi-momentum points in the Brillouin zone – the Dirac points. These points are topological defects in the band structure, with an associated Berry phase of  $\pm\pi$ . This warrants their stability with respect to lattice perturbations, so that a large range of lattice anisotropies only changes their position inside the Brillouin zone. In contrast, breaking the inversion symmetry of the potential by introducing an energy offset  $\Delta$  between sublattices opens an energy gap at the Dirac points, proportional to the offset. In our implementation, the sublattice offset  $\Delta$  depends only on the value of the phase  $\theta$  and can be precisely adjusted (see Methods). As displayed in Fig. 1c and d, the primitive lattice vectors are perpendicular, leading to a square Brillouin zone with two Dirac points inside. Their position is symmetric around the center and

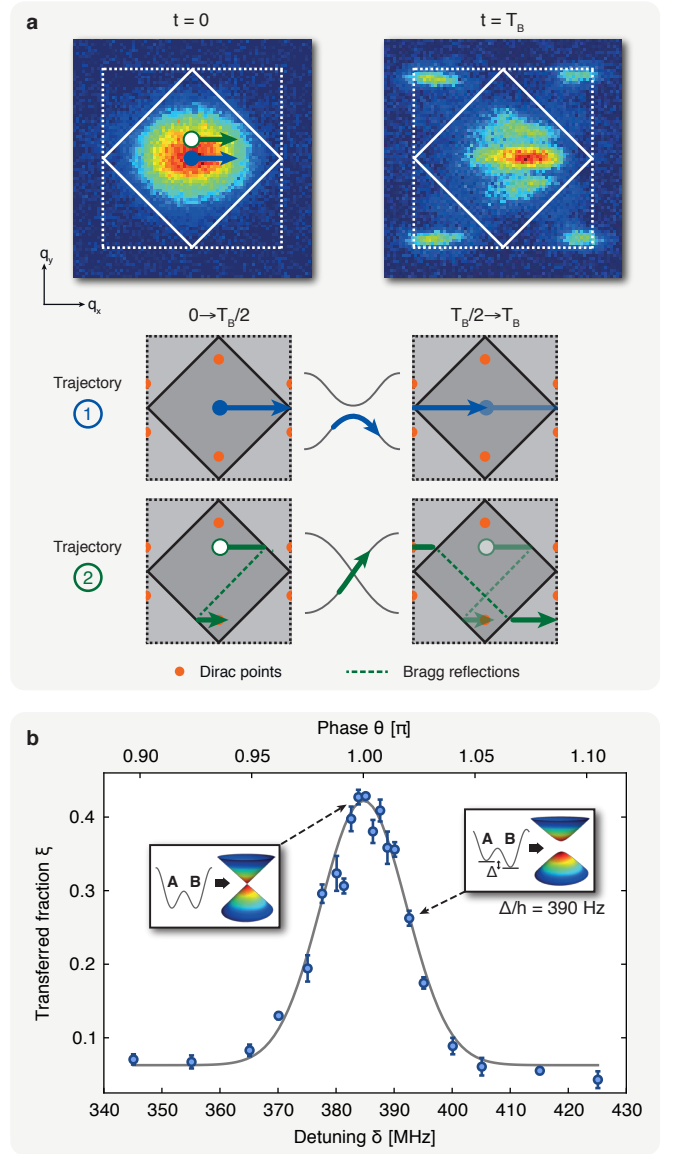


**FIG. 2: Probing the Dirac points.** **a**, Quasi-momentum distribution of the atoms before and after one Bloch oscillation of period  $T_B$ . The cloud explores several trajectories in quasi-momentum space simultaneously. For trajectory 1 (blue solid circle) the atoms remain in the first energy band. In contrast, trajectory 2 (green open circle) passes through a Dirac point at  $t = T_B/2$ . There, the energy splitting between the bands vanishes and the atoms are transferred to the second band. When measuring the quasi-momentum distribution at  $t = T_B$ , these atoms are missing in the first Brillouin zone and appear in the second one. **b**, Dependence of the total fraction of atoms transferred to the second band  $\xi$  on the detuning of the lattice beams  $\delta$ , which controls the sublattice energy offset  $\Delta$ . The maximum indicates the point of inversion symmetry, where  $\Delta = 0$  ( $\theta = \pi$  in eq. (1)) and the gap at the Dirac point vanishes. Away from the peak, the atoms behave as Dirac fermions with a tunable mass (see insets). Values and error bars denote the mean and standard deviation of five consecutive measurements, whereas the solid line is a Gaussian fit to the data.

fixed to  $q_x = 0$ , owing to the time-reversal and reflection symmetries of the system [19].

We characterise the Dirac points by probing the energy splitting between the two lowest energy bands through interband transitions [20]. The starting point of the experiment is a non-interacting ultracold gas of  $N \simeq 50,000$  fermionic  $^{40}\text{K}$  atoms in the  $|F, m_F\rangle = |9/2, -9/2\rangle$  state. The cloud is prepared in the lowest energy band of a honeycomb lattice with  $V_{\bar{X},X,Y}/E_R = [4.0(2), 0.28(1), 1.8(1)]$ , which also causes a weak harmonic confinement with trapping frequencies  $\omega_{x,y,z}/2\pi = [17.6(1), 31.8(5), 32.7(5)]$  Hz. Here  $E_R = \hbar^2/2m\lambda^2$ ,  $\hbar$  denotes the Planck constant and  $m$  the mass of  $^{40}\text{K}$ . By applying a weak magnetic field gradient, the atomic cloud is subjected to a constant force  $F$  along the  $x$  direction, equivalent to an electric field in solid-state systems. The atoms are hence accelerated such that their quasi-momentum  $q_x$  increases linearly up to the edge of the Brillouin zone, where a Bragg reflection occurs. The cloud eventually returns to the center of the band, performing one full Bloch oscillation [21]. We then measure the quasi-momentum distribution of the atoms in the different bands [22] (see Methods).

Owing to the finite momentum width of the cloud, trajectories with different quasi-momenta  $q_y$  are simultaneously explored during the Bloch cycle, as illustrated in Fig. 2a. For a trajectory far from the Dirac points, the atoms remain in the lowest energy band (trajectory 1). In contrast, when passing through a Dirac point (trajectory 2), the atoms are transferred from the first to the second band because of the vanishing energy splitting at the linear band crossing. When measuring the quasi-momentum distribution, these atoms are missing in the first Brillouin zone and appear in the second band, as can be seen in Fig. 2a. We identify the points of maximum transfer with the Dirac points. The energy resolution of the method is set by the characteristic energy of the applied force [21]  $E_B/\hbar = F\lambda/2\hbar = 88.6(7)$  Hz, which is small compared to the full bandwidth  $W/\hbar = 4.6$  kHz and the minimum band gap at the edges of the Brillouin zone  $E_G/\hbar = 475$  Hz.

To investigate how breaking the inversion symmetry of the lattice affects the Dirac points, we vary the sublattice offset  $\Delta$ , which is controlled by the frequency detuning  $\delta$  between the lattice beams, and measure the total fraction of atoms transferred to second band  $\xi$ . The results obtained for a honeycomb lattice with  $V_{\bar{X},X,Y}/E_R = [3.6(2), 0.28(1), 1.8(1)]$  are displayed in Fig. 2b, and show a sharp maximum in the transferred fraction. We identify this situation as the point of inversion symmetry  $\Delta = 0$  ( $\theta = \pi$ ), in good agreement with an independent calibration (see Methods). At this setting the band gap at the Dirac points vanishes. The population in the second band decreases symmetrically on both sides of the peak as the gap opens up, indicating the transition from massless to massive Dirac fermions.

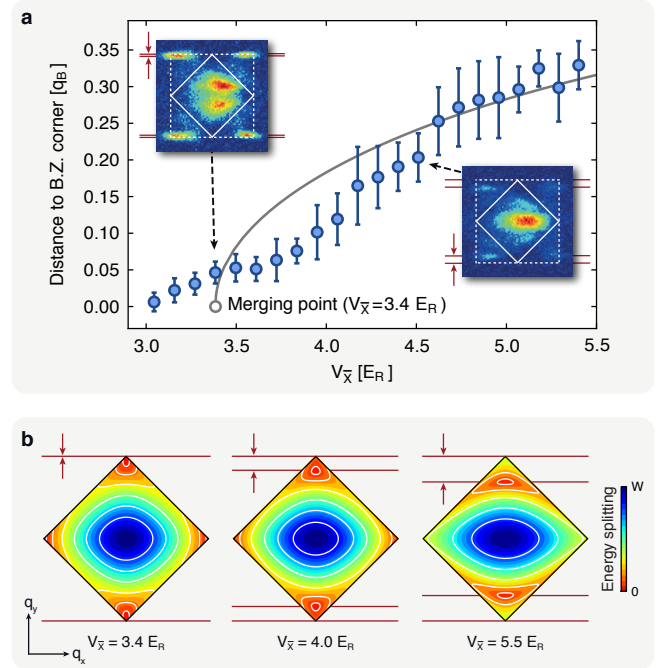


**FIG. 3: Movement of the Dirac points.** **a**, Distance of the Dirac points to the corners of the Brillouin zone, as measured through momentum-resolved interband transitions. The tunneling along the  $x$  direction increases when decreasing the lattice depth  $V_{\bar{X}}$ . The distance is extracted from the second band quasi-momentum distribution after one Bloch cycle (see insets). The merging of the two Dirac points at the corners of the Brillouin zone is signalled by a single line of missing atoms in the first band. Values and error bars are the mean and standard deviation of three to nine measurements. The solid line is the prediction of a two-dimensional band structure calculation without any fitting parameters. **b**, Energy splitting between the two lowest bands. It shows the displacement of the Dirac cones inside the Brillouin zone, as well as their deformation depending on the lattice depth  $V_{\bar{X}}$ .

The relative strength of the tunnel couplings between the different sites of the lattice fixes the position of the Dirac points inside the Brillouin zone, as well as the slope of the associated linear dispersion relation [5–9]. However, the tunability of our optical lattice structure allows for independent adjustment of the tunneling parameters along the  $x$  and  $y$  directions simply by controlling the intensity of the laser beams. For isotropic tunnelings the slope of the Dirac cones is the same in all directions, while being anisotropic otherwise. The distance of the Dirac points to the corners of the Brillouin zone along  $q_y$  can be varied between 0 and  $q_B/2$ , whilst  $q_x = 0$  due to reflection symmetry [19]. Here  $q_B = 2\pi/\lambda$  denotes the Bloch wave vector.

We exploit the momentum resolution of the interband transitions to directly observe the movement of the Dirac points. Starting from a honeycomb lattice with  $V_{\bar{X},X,Y}/E_R = [5.4(3), 0.28(1), 1.8(1)]$ , we gradually in-

crease the tunneling along the  $x$  direction by decreasing the intensity of the  $\bar{X}$  beam. As displayed in Fig. 3, the position of the Dirac points continuously approaches the corners of the Brillouin zone, as expected from an *ab initio* two-dimensional band structure calculation (see Methods).

When reaching the corners, the two Dirac points merge, annihilating each other. There, the dispersion relation becomes quadratic along the  $q_y$  axis, remaining linear along  $q_x$ . Beyond this critical point, a finite band gap appears for all quasi-momenta of the Brillouin zone. This situation signals the transition between band structures of two different topologies, one containing two Dirac points and the other none. For two-dimensional honeycomb lattices at half filling, it corresponds to a Lifshitz phase transition from a semi-metallic to a band-insulating phase [6, 7].

We experimentally map out the topological transition line by recording the fraction of atoms transferred to the second band  $\xi$  as a function of the lattice depths  $V_{\bar{X}}$  and  $V_X$ , while keeping  $V_Y/E_R = 1.8(1)$ . The results are displayed in Fig. 4a. There, the onset of population

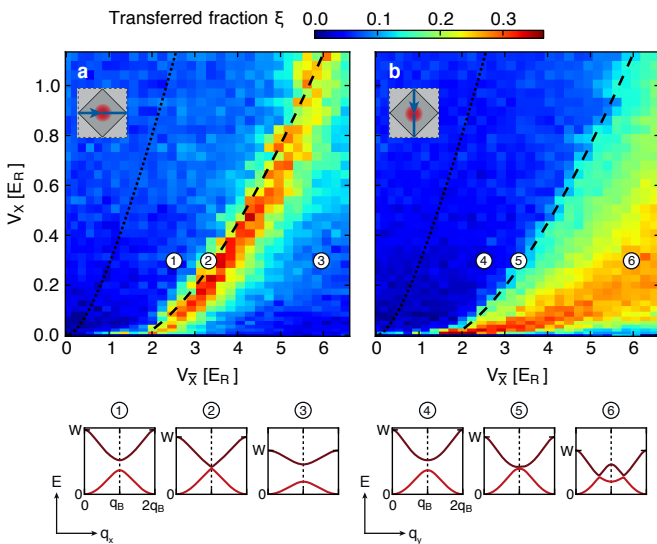


FIG. 4: **Topological transition.** Fraction of atoms transferred to the second band  $\xi$  as a function of lattice depths  $V_{\bar{X}}$  and  $V_X$ , with  $V_Y/E_R = 1.8(1)$ . Different lattice geometries (square, chequerboard, triangular, dimer and honeycomb) are realised, see Fig. 1b. We consider trajectories in quasi-momentum space along the  $q_x$  and  $q_y$  directions (a and b resp.). To maximise the transfer for the  $q_y$  trajectories, where the cloud successively passes the two Dirac points, we set  $\theta = 1.013(1)\pi$ . In both cases, the onset of population transfer to the second band signals the topological transition, where the Dirac points appear. The dashed line is the theoretical prediction for the transition line without any fitting parameters. The insets show cuts of the band structure along the  $q_y$  axis ( $q_x = 0$ ), illustrating the emergence of the Dirac points when increasing  $V_{\bar{X}}$ .

transfer to the second band signals the appearance of Dirac points in the band structure of the lattice. The transferred fraction  $\xi$  decreases for large values of  $V_{\bar{X}}$ , as the Dirac point positions exceed the momentum width of the cloud.

To extend the range of our measurements and probe the Dirac points even in this regime, we apply a force along the  $y$  direction. We hence explore a new class of trajectories in quasi-momentum space. This allows for the investigation of very anisotropic Dirac cones, which become almost flat along the  $q_x$  direction as we approach the crossover to a one-dimensional lattice structure ( $V_{\bar{X}} \gg V_X$ ). Along the  $q_y$  trajectories the center of the cloud successively passes the two Dirac points during the Bloch cycle, effectively realising a Stückelberg interferometer [23, 24] in a two-dimensional band structure. As displayed in Fig. 4b, we again identify the topological transition through the onset of population transfer to the second band. The results for the transition line obtained for both measurement series are in excellent agreement with *ab initio* band structure calculations.

In this work we have realised Dirac points with highly tunable properties using ultracold fermionic atoms in a honeycomb optical lattice. A new class of physical phenomena is now within the domain of quantum gas experiments. Furthermore, the flexibility and novel observables of these systems will provide new insights. For example, the unique coherence of quantum gases offers the possibility of directly measuring the Berry phase associated to the Dirac points by interferometric methods. Topological order could be achieved by introducing artificial gauge fields, either via Raman transitions [25] or time-dependent lattice modulation [26]. Moreover, the exceptionally tunable lattice potential we have developed opens up a wealth of new avenues for optical lattice experiments. For spin mixtures with repulsive interactions, the dynamic transition between dimer and square lattices should facilitate the adiabatic preparation of an anti-ferromagnetic phase [27] and enable the study of quantum criticality [28]. Additionally, the triangular and honeycomb lattices provide the possibility to explore magnetic frustration and spin liquid phases [11, 12].

## METHODS

**Preparation scheme.** After sympathetic cooling with  $^{87}\text{Rb}$  in a magnetic trap,  $2 \times 10^6$  fermionic  $^{40}\text{K}$  atoms are transferred into a dipole trap operating at a wavelength of 826 nm. A balanced spin mixture of the  $|F, m_F\rangle = |9/2, -9/2\rangle$  and  $|9/2, -7/2\rangle$  states is evaporatively cooled at a magnetic field of 197.6(1) G, in the vicinity of the Feshbach resonance at 202.1 G. We obtain typical temperatures of  $0.2 T_F$ , where  $T_F$  is the Fermi temperature. The field is subsequently reduced and a magnetic field gradient is used to selectively remove the

$|9/2, -7/2\rangle$  component, while levitating the  $|9/2, -9/2\rangle$  atoms against gravity. This polarised Fermi gas is loaded into the two-dimensional optical lattice within 200 ms, and the dipole trap is then switched off.

**Tunable optical lattice.** The optical lattice is produced by the combination of three retro-reflected laser beams of linear polarization and wavelength  $\lambda = 1064$  nm, red detuned with respect to the  $D_1$  and  $D_2$  lines of  $^{40}\text{K}$ . The  $\bar{X}$  and  $X$  beams propagate along the same axis, while the  $Y$  beam is at  $90.0(1)$ . The interference of the  $X$  and  $Y$  beams produces a checkerboard potential of the form [29]  $V_1(x, y) = -V_X \cos^2(kx) - V_Y \cos^2(ky) - 2\alpha\sqrt{V_X V_Y} \cos(kx) \cos(ky) \cos\varphi$ . The phase between the two beams at the position of the atoms is stabilised interferometrically to  $\varphi/\pi = 0.00(3)$  using a pair of additional beams detuned from each other and from  $\bar{X}$ ,  $X$  and  $Y$ . This results in a weak additional lattice along each axis of about  $0.1E_R$ . The  $\bar{X}$  beam creates a potential  $V_2(x) = -V_{\bar{X}} \cos^2(kx + \theta/2)$ , where the phase  $\theta$  determines the relative position of the checkerboard pattern and the one-dimensional standing wave. We control the value of  $\theta$  in the center of the cloud by adjusting the frequency detuning  $\delta$  between the  $\bar{X}$  and  $X$  beams. We infer the precise value  $\theta/\delta = [\pi/384.7(6)] \text{ MHz}^{-1}$  from the peak position in Fig. 2b. This is in good agreement with an independent calibration obtained using Raman-Nath diffraction on a  $^{87}\text{Rb}$  Bose-Einstein condensate, which yields  $\theta/\delta = [\pi/388(4)] \text{ MHz}^{-1}$ . At the edges of the cloud the phase differs by approximately  $\pm 10^{-4}\pi$ . The total lattice potential is given by  $V_1(x, y) + V_2(x)$  and, depending on the relative intensities of the beams, gives rise to square, checkerboard, triangular and honeycomb lattices, as well as a staggered arrangement of dimers [30] and an array of weakly coupled one-dimensional chains. The visibility  $\alpha = 0.90(5)$  and the lattice depths  $V_{\bar{X}, X, Y}$  are calibrated by Raman-Nath diffraction. The method has a systematic uncertainty of 10% for the lattice depths, whereas the statistical uncertainties are given in the main text. The two-dimensional lattice lies in the  $xy$  plane, whereas in the  $z$  direction the atoms are harmonically trapped. Owing to the absence of interactions the  $z$  direction decouples. The underlying trap frequencies in our system scale with the lattice depths according to the approximate expressions  $\omega_x \propto \sqrt{V_Y}$ ,  $\omega_y \propto \sqrt{V_{\bar{X}} + (V_X V_Y / V_{\bar{X}})}$  and  $\omega_z \propto \sqrt{V_{\bar{X}} + (V_X V_Y / V_{\bar{X}})} + 1.24V_Y$ . For the measurements in Fig. 2a we find  $\omega_{x,y,z}/2\pi = [17.6(1), 31.8(5), 32.7(5)] \text{ Hz}$ , as calibrated from dipole oscillations of the cloud.

**Detection.** The quasi-momentum distribution of the gas is probed using a band-mapping technique. The optical lattice beams are linearly ramped down in  $500 \mu\text{s}$ , slowly enough for the atoms to stay adiabatically in their band while quasi-momentum is approximately conserved [22]. We then allow for 15 ms of ballistic expansion before taking an absorption image of the cloud.

**Band structure calculations.** The energy spec-

trum is obtained using an *ab initio* single-particle two-dimensional numerical band structure calculation for the homogeneous system. It therefore also takes into account higher order tunneling terms, which are relevant for the regime explored in this paper. In particular, they cause an asymmetry between the two lowest bands and lead to a tilt of the Dirac cones for certain parameter regimes.

- 
- [1] Castro Neto, A. H., Guinea, F., Peres, N. M. R., Novoselov, K. S. & Geim, A. K. The electronic properties of graphene. *Rev. Mod. Phys.* **81**, 109–162 (2009).
  - [2] Hasan, M. Z. & Kane, C. L. Colloquium: Topological insulators. *Rev. Mod. Phys.* **82**, 3045–3067 (2010).
  - [3] Bloch, I., Dalibard, J. & Zwerger, W. Many-body physics with ultracold gases. *Rev. Mod. Phys.* **80**, 885–964 (2008).
  - [4] Esslinger, T. Fermi-Hubbard Physics with Atoms in an Optical Lattice. *Annu. Rev. Condens. Matter Phys.* **1**, 129–152 (2010).
  - [5] Hasegawa, Y., Konno, R., Nakano, H. & Kohmoto, M. Zero modes of tight-binding electrons on the honeycomb lattice. *Phys. Rev. B* **74**, 033413 (2006).
  - [6] Zhu, S.-L., Wang, B. & Duan, L.-M. Simulation and Detection of Dirac Fermions with Cold Atoms in an Optical Lattice. *Phys. Rev. Lett.* **98**, 260402 (2007).
  - [7] Wunsch, B., Guinea, F. & Sols, F. Dirac-point engineering and topological phase transitions in honeycomb optical lattices. *New J. Phys.* **10**, 103027 (2008).
  - [8] Montambaux, G., Piéchon, F., Fuchs, J.-N. & Goerbig, M. O. Merging of Dirac points in a two-dimensional crystal. *Phys. Rev. B* **80**, 153412 (2009).
  - [9] Lee, K. L., Grémaud, B., Han, R., Englert, B.-G. & Miniatura, C. Ultracold fermions in a graphene-type optical lattice. *Phys. Rev. A* **80**, 043411 (2009).
  - [10] Pereira, V. M., Castro Neto, A. H. & Peres, N. M. R. Tight-binding approach to uniaxial strain in graphene. *Phys. Rev. B* **80**, 045401 (2009).
  - [11] Balents, L. Spin liquids in frustrated magnets. *Nature* **464**, 199–208 (2010).
  - [12] Meng, Z. Y., Lang, T. C., Wessel, S., Assaad, F. F. & Muramatsu, A. Quantum spin liquid emerging in two-dimensional correlated Dirac fermions. *Nature* **464**, 847–851 (2010).
  - [13] Giorgini, S., Pitaevskii, L. P. & Stringari, S. Theory of ultracold atomic Fermi gases. *Rev. Mod. Phys.* **80**, 1215–1274 (2008).
  - [14] Jördens, R., Strohmaier, N., Günter, K., Moritz, H. & Esslinger, T. A Mott insulator of fermionic atoms in an optical lattice. *Nature* **455**, 204–207 (2008).
  - [15] Schneider, U. *et al.* Metallic and Insulating Phases of Repulsively Interacting Fermions in a 3D Optical Lattice. *Science* **322**, 1520–1525 (2008).
  - [16] Soltan-Panahi, P. *et al.* Multi-component quantum gases in spin-dependent hexagonal lattices. *Nature Phys.* **7**, 434–440 (2011).
  - [17] Soltan-Panahi, P., Lühmann, D.-S., Struck, J., Windpassinger, P. & Sengstock, K. Quantum phase transition to unconventional multi-orbital superfluidity in optical lattices. *Nature Phys.* in press (2011).

- [18] Salger, T., Geckeler, C., Kling, S. & Weitz, M. Atomic Landau-Zener Tunneling in Fourier-Synthesized Optical Lattices. *Phys. Rev. Lett.* **99**, 190405 (2007).
  - [19] Asano K. & Hotta, C. Designing Dirac points in two-dimensional lattices. *Phys. Rev. B* **83**, 245125 (2011).
  - [20] Anderson, B. P. & Kasevich, M. A. Macroscopic Quantum Interference from Atomic Tunnel Arrays. *Science* **282**, 1686–1689 (1998).
  - [21] Ben Dahan, M., Peik, E., Reichel, J., Castin, Y. & Salomon, C. Bloch Oscillations of Atoms in an Optical Potential. *Phys. Rev. Lett.* **76**, 4508–4511 (1996).
  - [22] Köhl, M., Moritz, H., Stöferle, T., Günter, K. & Esslinger, T. Fermionic Atoms in a Three Dimensional Optical Lattice: Observing Fermi Surfaces, Dynamics, and Interactions. *Phys. Rev. Lett.* **94**, 080403 (2005).
  - [23] Kling, S., Salger, T., Grossert, C. & Weitz, M. Atomic Bloch-Zener Oscillations and Stückelberg Interferometry in Optical Lattices. *Phys. Rev. Lett.* **105**, 215301 (2010).
  - [24] Zenesini, A., Ciampini, D., Morsch, O. & Arimondo, E. Observation of Stückelberg oscillations in accelerated optical lattices. *Phys. Rev. A* **82**, 065601 (2010).
  - [25] Lin, Y.-J., Compton, R. L., Jiménez-García, K., Porto, J. V. & Spielman, I. B. Synthetic magnetic fields for ultracold neutral atoms. *Nature* **462**, 628–632 (2009).
  - [26] Kitagawa, T., Berg, E., Rudner, M. & Demler, E. Topological characterization of periodically driven quantum systems. *Phys. Rev. B* **82**, 235114 (2010).
  - [27] Lubasch, M., Murg, V., Schneider, U., Cirac, J. I. & Bañuls, M.-C. Adiabatic Preparation of a Heisenberg Antiferromagnet Using an Optical Superlattice. *Phys. Rev. Lett.* **107**, 165301 (2011).
  - [28] Sachdev, S. Quantum magnetism and criticality. *Nature Phys.* **4**, 173–185 (2008).
  - [29] Hemmerich A., Schropp, D., Esslinger, T. & Hänsch, T. W. Elastic Scattering of Rubidium Atoms by Two Crossed Standing Waves. *Europhys. Lett.* **18**, 391–395 (1992).
  - [30] Sebby-Strabley, J., Anderlini, M., Jessen, P. S. & Porto, J. V. Lattice of double wells for manipulating pairs of cold atoms. *Phys. Rev. A* **73**, 033605 (2006).
- Acknowledgements.** We would like to thank D. Poletti for bringing our attention to honeycomb lattices without six-fold symmetry, and N. Cooper and F. Hassler for insightful discussions. We acknowledge SNF, NCCR-MaNEP, NCCR-QSIT, NAME-QUAM (EU, FET open), SQMS (ERC advanced grant) and ESF (POLATOM) for funding.
- Author Contributions.** The data was taken and analysed by L.T., D.G., T.U. and G.J. The tunable optical lattice was built by D.G. The experimental concept was developed by T.E. All authors contributed extensively to the discussion of the results, as well as to the preparation of the manuscript.
- Author Information.** Correspondence and requests for materials should be addressed to T.E. (esslinger@phys.ethz.ch).